High-Q plasmonic and dielectric modes in a metal-coated whispering-gallery microcavity

You-Ling Chen,[1] Chang-Ling Zou,[2] Yi-Wen Hu,[1] and Qihuang Gong[1,*]

[1]*State Key Lab for Mesoscopic Physics and Department of Physics, Peking University, Beijing 100871, P. R. China*

[2]*Key Lab of Quantum Information, University of Science and Technology of China, Hefei 230026, P. R. China*

(Received 12 December 2012; published 20 February 2013)

This paper investigates the confinement and quality (Q) factors of the dielectric mode, exterior surface plasmonic mode, and interior surface plasmonic mode in a metal-nanolayer-coated silica microtoroid. It is found that the confinement of these modes relies mainly on the real part of the coating-metal permittivity, and a smaller negative real part produces a lower effective potential barrier which plays distinct roles in these three types of modes. For the exterior plasmonic mode, a lower potential leads to a better confinement and thus lower radiation losses, while for the interior plasmonic mode and the dielectric mode, a higher potential can play a very positive role in suppressing the radiation losses. The metal absorption loss, as expected, is directly related to the imaginary part of the metal permittivity and the energy fraction of the mode in the metal layer, and the latter depends on the confinement or, namely, the effective potential barrier induced by the metal nanolayer. We also compare the plasmonic modes in the coated microcavity and the dielectric modes in the uncoated microcavity at different cavity sizes. An interesting finding is that when the cavity is small enough, which is highly desirable for compact photonic devices, the Q factors of the plasmonic modes even exceed significantly that of the uncoated dielectric modes.

DOI: 10.1103/PhysRevA.87.023824 PACS number(s): 42.60.Da, 42.79.−e, 73.20.Mf

I. INTRODUCTION

Surface plasmon polaritons (SPPs) have attracted much attention recently due to their great potential in highly concentrating and channeling light in subwavelength structures [1–3]. The strongly localized optical fields in these plasmonic devices are of importance in the emerging field of nanophotonics [4], such as surface-enhanced Raman spectroscopy [5–7], surface-enhanced fluorescence [8,9], and optical chemical or biological sensors [10–15]. Over the past few years, plasmonic resonators [16–19] have been demonstrated to play an important role in miniaturized photonic circuit and further enhanced light-matter interaction with specific applications towards light sources and ultrasensitive biosensors at nanoscale. So far, various plasmonic resonators with different geometrical designs have been reported, including periodic optical Bragg mirrors [18,20–24], annular nanoresonators [25], the metallic nanowire Fabry-Perot (FP) resonator [16], the sandwiched FP-type nanocavity [17], the metallic fin FP resonator [26], the metallic torus-dielectric-metallic flat surface resonator [27], the silver disk-dielectric disk-silver disk resonator [28], and the ring-type V-groove microresonator [29,30]. Unfortunately, their quality (Q) factors are typically smaller than 100 in both visible and near-infrared wavelengths [16–19], which are far below the theoretical values limited by the intrinsic loss of metal at room temperature.

Recently, Min *et al*. demonstrated experimentally a plasmonic microcavity fabricated by coating the surface of a high-Q silica microdisk [31,32] with a thin layer of silver [33]. With the form of whispering-gallery modes, the experimental Q factors of plasmonic modes exceed 1000 in the near infrared at room temperature, which are close to the theoretical metal-loss-limited Q factors. Nevertheless, the plasmonic modes studied in Ref. [33] are located in the interior surface of the metal layer, and are not easy to interact with the surrounding medium. Against this backdrop, Xiao *et al*. proposed a kind of whispering-gallery plasmonic modes which are highly concentrated on the exterior surface of a metal-coated microtoroid [34]. This exterior surface mode possesses high-Q factors comparable to that of the interior mode at room temperature. However, more studies on the exterior and interior plasmonic modes are in urgent need. For example, their confinement mechanisms deserve to be further revealed, and the Q factors need an improvement. In this paper, we provide systematic study on the physics behind the Q factors of the dielectric and plasmonic modes supported by a metal-coated microtoroid.

The paper is organized as follows. Section II depicts the model and studies the mode dispersion of the dielectric and plasmonic modes in a metal-coated whispering-gallery microtoroid resonator. Section III shows that the real and imaginary parts of the relative permittivity of the coating metal play different roles in the Q factors of the dielectric, interior plasmonic, and exterior plasmonic modes. On one hand, with a given real part, the Q factor increases rapidly when the imaginary part gets smaller. On the other hand, for a given imaginary part, the Q factors of the three kinds of modes change distinctly with the real part because of different confinement mechanisms. In Sec. IV, we focus on the impact of the operation wavelength on the Q factors of the plasmonic modes. Section V compares the plasmonic and the uncoated dielectric modes at different cavity sizes. A counterintuitive finding is that when the cavity radius approaches only several micrometers, which is highly desirable for compact photonic devices, the Q factors of the plasmonic modes even exceed significantly that of the uncoated dielectric modes. Finally, Sec. VI provides a short conclusion and a brief discussion.

II. MODEL

The geometry of the present microresonator system is depicted in Fig. 1, similar to Ref. [34]. A silica microtoroid [35], with permittivity $\varepsilon_{\text{silica}} = n^2_{\text{silica}}$ and the major (minor)

*qhgong@pku.edu.cn

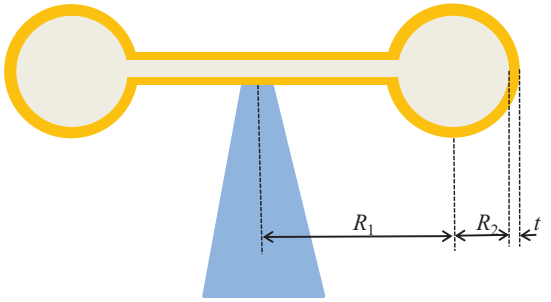

FIG. 1. (Color online) Side view of the proposed system. A core silica microtoroid (shown in gray) on a silicon wafer (shown in blue) is coated by a nanolayer of metal (shown in yellow). R_1 and R_2 are the major and minor radii of the silica toroid, and t denotes the coating thickness of metal. R_2 and t are fixed at 1 μm and 100 nm throughout the paper.

radius R_1 (R_2), is coated by a thin layer of metal with permittivity ε, e.g., silver. For some applications such as optical sensing, the coated microtoroid may be embedded in a surrounding material with permittivity $\varepsilon_{\text{surr}}$. Throughout this paper, the term permittivity denotes the dimensionless relative permittivity. In experiment, the silica microtoroid on a silicon wafer can be prepared by standard photolithography and etchings followed by a CO_2 laser-assisted reflow process described in Ref. [36]. The silver coating can be deposited on the template silica microtoroid using a sputtering technique. Feasible experimental data for the major and minor radii of the microtoroid are around 5–100 and 1–5 μm, respectively. To better expose the plasmonic modes, throughout this paper, R_2 is fixed at 1 μm. The coating thickness of metal t is chosen to be 100 nm for two reasons. First, this thickness is quite easy to prepare experimentally. Second, this thickness is beneficial for the independent excitation of either the exterior or interior plasmonic mode, and so favorable for our study of the confinement mechanisms of the modes. The surrounding material is supposed to be water.

Generally, whispering-gallery modes supported by this kind of rotational-symmetric microstructure can be identified by three mode parameters in addition to their transverse electric (TE) or transverse magnetic (TM) polarization: the radial mode number n, the angular mode number l, and the azimuthal mode number m. As the fundamental modes possess best properties, e.g., the largest Q factor and the smallest mode volume V, we focus on the fundamental modes, i.e., $n = 1$, $m = l$.

To analyze quantitatively the mode confinement mechanism of the aforementioned system, we study the mode dispersion of the three kinds of fundamental modes: the dielectric eigenmodes, interior plasmonic eigenmodes, and exterior plasmonic eigenmodes. A full-vectorial finite element (FEM) [37,38] analysis is performed by taking into account the material dispersion of silver [39] while neglecting that of silica [40] and water [41,42]. Details of the FEM simulation can be found in the Appendix. Figure 2 plots the real part of the eigenfrequencies f as a function of the azimuthal mode number m. The vacuum light line and silica light line are defined by $f = mc/(2\pi R_b)$ and $f = mc/(2\pi n_{\text{silica}} R_b)$, respectively, where c is the vacuum light speed, and $R_b = R_1 + R_2 + t$ stands for the total boundary radius of the coated

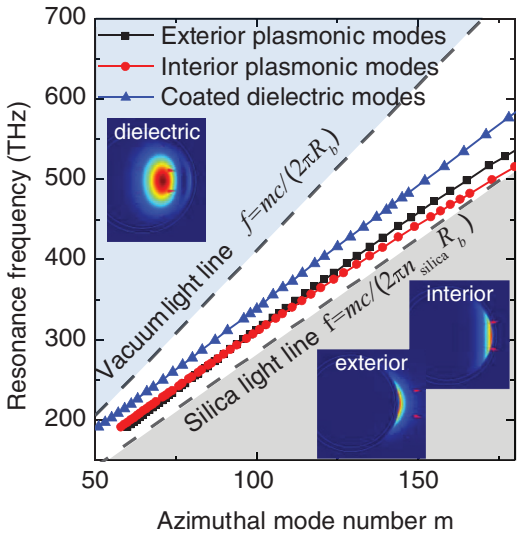

FIG. 2. (Color online) Numerically simulated cavity mode dispersion diagrams for fundamental dielectric mode, interior plasmonic mode, and exterior plasmonic mode. The major radius of the silver-coated silica microtoroid $R_1 = 10$ μm. The upper and lower black dashed lines correspond to the vacuum and silica light lines, respectively. Insets show magnetic energy-density profiles in the transverse plane using a false-color map for these three kinds of cavity modes.

microtoroid. As pointed out by Ref. [33], the eigenmodes of the coated microcavity can be classified into two distinctive categories. One is the optical dielectric mode with the strongest field located in the silica ring (in this paper, we only consider the TM-polarized mode unless specified), which results from the dielectric waveguide channel; the other belongs to surface-plasmonic mode confined at the metal-dielectric interface. The main difference compared to Ref. [33] is that not only the metal-silica interface but also the metal-water interface support well-localized plasmonic modes, which is studied in Ref. [34].

III. EFFECT OF THE METAL PERMITTIVITY ON THE Q FACTORS

We now analyze the Q factors of plasmonic and dielectric modes in this kind of whispering-gallery microcavity. In Refs. [33,34], authors studied the Q factors of either the interior or exterior plasmonic whispering gallery modes when the coated metal was silver. Nevertheless, the role of the permittivity of the metal has not been revealed completely although it is well known that the imaginary part describes the absorption loss of metal. In particular, it remains unclear whether there is a set of optimal coating parameters for achieving higher-Q factors compared to that in Refs. [33,34]. With the technique of metamaterial [43], it is possible to synthesize materials with permittivity unattainable in nature. In this section, instead of a certain kind of metal, we assume a generalized permittivity of the coating metal denoted by $\varepsilon = \text{Re}[\varepsilon] + i\,\text{Im}[\varepsilon]$, which allows for exploring the underlying physics. Throughout this section, R_1 is set as 10 μm, and the wavelength of interest is 680 nm.

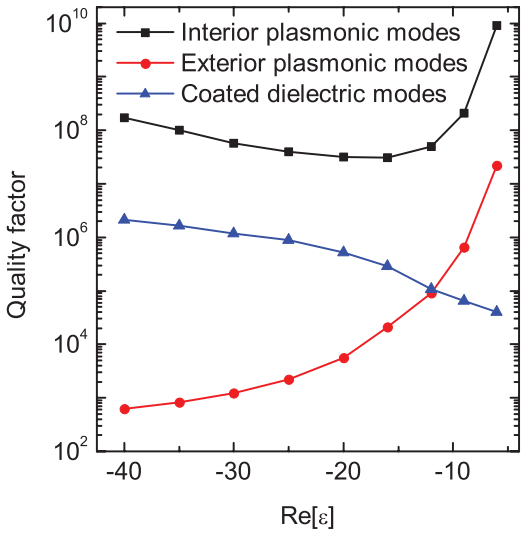

FIG. 3. (Color online) Numerically simulated Q factors depending on Re[ε] in the case of Im[ε] = 0 for the interior plasmonic modes, the exterior plasmonic modes, and the dielectric modes.

A. Purely real permittivity of the coating metal

For simplicity, we first study the special case of a purely real permittivity, i.e., Im[ε] = 0, which provides the convenience to reveal the role of Re[ε]. In this case, the Q factor is attributed to the radiation loss since the metal absorption has been totally removed. The numerically simulated Q factors for the three types of fundamental modes depending on Re[ε] are shown in Fig. 3. On one hand, it can be found that, with a smaller negative real part, the Q factors of the dielectric mode and exterior plasmonic mode decrease and increase monotonically, respectively. Specifically, when $|\mathrm{Re}[\varepsilon]| < 12$, the Q factor of the exterior plasmonic mode even exceeds that of the dielectric mode. On the other hand, the Q factor of the interior counterpart decreases first and then increases, and it is much higher than that of the other two kinds of modes.

To explain the two points described above, we employ the effective potential approach [44]. By making an analogy of the Helmholtz equation to the radial Schrödinger equation (two dimensional), the effective radial potential of the whispering-gallery mode can be expressed by

$$V_{\mathrm{eff}}(r) = k^2[1 - \varepsilon(r)] + \frac{l^2}{r^2}, \tag{1}$$

where $k = 2\pi/\lambda$ is the vacuum wave number, $\varepsilon(r)$ is the material permittivity at the radial position r, and l is the azimuthal mode number. The first term $k^2[1 - \varepsilon(r)]$ describes the permittivity discontinuity at the interfaces, and the second term l^2/r^2 is the centrifugal potential. The interior and exterior plasmonic modes propagate along the metal-silica and metal-water interfaces, respectively. Unlike the pure dielectric whispering-gallery microcavity, the large negative value of Re[ε] of the coating metal forms a high potential barrier inside the resonator. Figure 4 plots the unitary effective potential $V_{\mathrm{eff}}(r)/k^2$ for the exterior plasmonic modes at different Re[ε]. The potential barriers for the interior plasmonic and dielectric modes are similar and not shown here. For all these three kinds of modes, the potential barrier turns lower with the decrease of $|\mathrm{Re}[\varepsilon]|$.

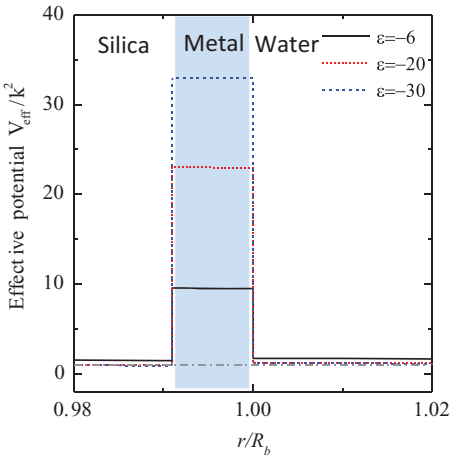

FIG. 4. (Color online) Effective potential for the exterior plasmonic modes when the pure real permittivities of coating metal are −6, −20, and −30, respectively. Here, the major radius of the toroid is 10 μm, and the resonant wavelength is in the 680-nm band.

The dependence of Q factor on Re[ε] for these three kinds of modes can be explained physically as follows. First, for the exterior plasmonic mode confined at the metal-surrounding dielectric surface, when $|\mathrm{Re}[\varepsilon]|$ is smaller, the potential barrier becomes lower as shown in Fig. 4. As a result, more mode energies can tunnel into the metal nanolayer, which produces a larger kinetic momentum of light for the mode. Therefore, the photons are more difficult to escape from the cavity due to the large photon momentum mismatch between the cavity mode and the free surrounding medium mode. In other words, a higher-Q factor related to the radiation loss can be expected for a smaller $|\mathrm{Re}[\varepsilon]|$ of the metal (mechanism I). Second, for the dielectric mode distributed in the silica core, as $|\mathrm{Re}[\varepsilon]|$ becomes smaller, a lower potential barrier increases the radiation loss of the mode and reduces the Q factor (mechanism II). Finally, it is more complicated for the interior plasmonic mode. This mode propagates along the metal-silica interface. On one hand, a lower potential barrier resulting from a smaller $|\mathrm{Re}[\varepsilon]|$ induces an increased radiation loss (mechanism II), similar to that occurred in the pure dielectric mode. On the other hand, the interior plasmonic mode turns to tunnel into the metal nanolayer when the potential barrier is low, which produces a large kinetic momentum of light and is beneficial for suppressing the radiation loss (mechanism I), similar to the effect in exterior plasmonic mode. Therefore, there is a balance of these two mechanisms.

The above analysis can be verified numerically. We plot the effective mode indices defined by $n_{\mathrm{eff}} = mc/(2\pi f R_b)$ for the three types of fundamental modes, as shown in Fig. 5(a). It can be seen that the indices of the interior and exterior plasmonic modes increase slowly by decreasing $|\mathrm{Re}[\varepsilon]|$ from 40, but speed up rapidly when $|\mathrm{Re}[\varepsilon]|$ is small, while the index of the dielectric mode is smaller than that of plasmonic modes and remains almost unchanged. For instance, the indices approach 1.75 and 1.58 when Re[ε] = −6 for the interior and exterior modes, respectively. These can also be demonstrated in Fig. 5(b) where the magnetic energy-density profiles of modes are shown for Re[ε] = −6 and −30. It is found that the coating metal with a smaller $|\mathrm{Re}[\varepsilon]|$ (e.g., Re[ε] = −6)

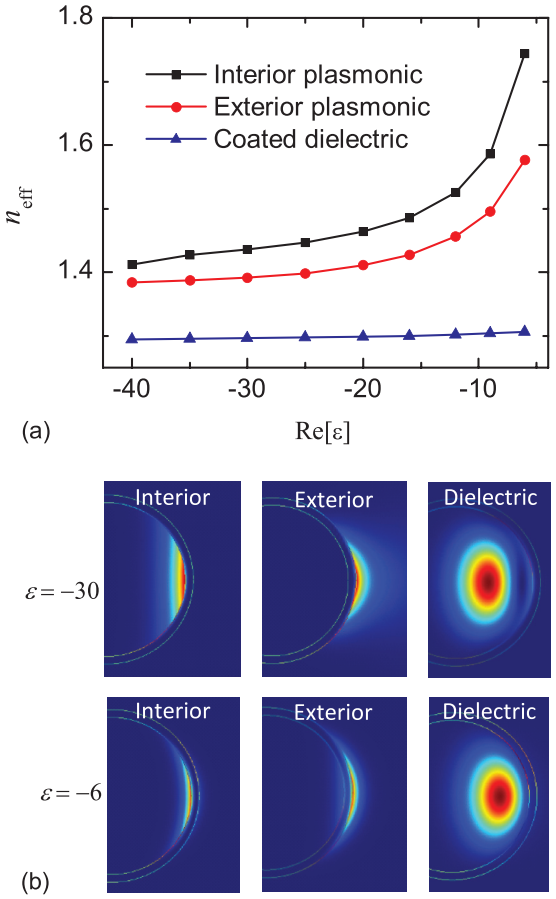

FIG. 5. (Color online) (a) Effective mode indices for the three kinds of modes depending on the purely real permittivity ε of the coating metal ($\mathrm{Im}[\varepsilon] \equiv 0$). (b) The upper and bottom panels show the magnetic energy-density profiles of the modes for $\varepsilon = -30$ and -6, respectively.

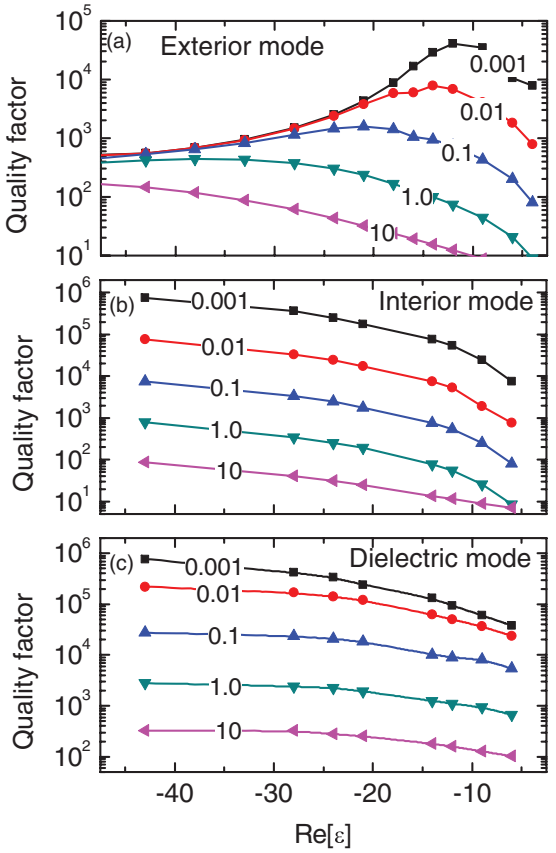

FIG. 6. (Color online) Q factors of the exterior plasmonic mode (a), the interior plasmonic mode (b), and the dielectric mode (c) for different $\mathrm{Im}[\varepsilon]$ of -0.001, -0.01, -0.1, -1, and -10.

shows much better confinement for the plasmonic modes, while there is not much difference for the dielectric mode. Note that the mode index describes the kinetic momentum of light for the corresponding mode. Thus, we have the following points. (i) For the exterior plasmonic mode, the Q factor keeps increasing because the mode index rises when $|\mathrm{Re}[\varepsilon]|$ decreases, and this increase accelerates when $|\mathrm{Re}[\varepsilon]|$ is small, governed by mechanism I. (ii) For the dielectric mode, the Q factor decreases monotonically by decreasing $|\mathrm{Re}[\varepsilon]|$ because mechanism II is dominant in this process. (iii) For the interior plasmonic mode, the Q factor shows an initial decrease when $\mathrm{Re}[\varepsilon]$ is from -40 to -16 since mechanism II dominates, while it exhibits an increase from -16 to -4 because mechanism I plays a more important role due to the rapidly enhanced mode index.

B. Complex permittivity of the coating metal

We now go on to explore the effect of the imaginary part of the coating-metal permittivity. When $\mathrm{Im}[\varepsilon] \neq 0$, the total Q factor Q_{total} consists of two contributions: Q_{rad} resulting from the radiation loss studied in the last section and Q_{abs} induced by intrinsic metal absorption, which is expressed by $Q_{\mathrm{total}}^{-1} = Q_{\mathrm{abs}}^{-1} + Q_{\mathrm{rad}}^{-1}$. Figures 6(a)–6(c) plot Q_{total} of the three types of fundamental modes for different metal permittivities. From these results, we can find the following points.

(i) It is straightforward that for a given real part of permittivity, a smaller imaginary part $\mathrm{Im}[\varepsilon]$ predicts a larger Q_{total} since $\mathrm{Im}[\varepsilon]$ describes the metal absorption. For example, Q_{total} of the exterior plasmonic mode can approach 10^5 when $\mathrm{Im}[\varepsilon] = -0.001$, and it falls to 10^4 and 10^3 when $\mathrm{Im}[\varepsilon] = -0.01$ and -0.1, respectively.

(ii) For the exterior plasmonic mode and the small imaginary part such as $\mathrm{Im}[\varepsilon] = -0.001$, -0.01, and -0.1, Q_{total} increases first and then decreases when the negative real part $\mathrm{Re}[\varepsilon]$ changes from -40 to -4, as shown in Fig. 6(a). This is because during this entire process the radiation loss decreases (studied in Fig. 3) while the metal absorption loss increases due to more and more mode energies tunneled in the coating-metal nanolayer. In more details, the radiation loss is dominant when $|\mathrm{Re}[\varepsilon]|$ remains large enough such as $|\mathrm{Re}[\varepsilon]| > 20$, and the Q factor is radiation limited, which can be demonstrated by the fact that Q_{total} has no such difference for $\mathrm{Im}[\varepsilon] = -0.001$, -0.01, and -0.1, while the metal absorption plays a more significant role when $|\mathrm{Re}[\varepsilon]| < 20$, and the Q factor is absorption limited in this case. Thus, there is an optimal $\mathrm{Re}[\varepsilon]$ for achieving the highest Q_{total} for $\mathrm{Im}[\varepsilon] = -0.001$, -0.01, and -0.1. When the imaginary part is large, e.g., $\mathrm{Im}[\varepsilon] = -10$, however, Q_{total} decreases monotonically because the metal absorption remains dominant when $\mathrm{Re}[\varepsilon]$ ranges from -40 to -4.

(iii) For the interior plasmonic mode, unlike the phenomena in Fig. 3, the total Q factor keeps degrading when Re[ε] ranges from -40 to -4, with the imaginary part ranging from -0.001 to -10, as shown in Fig. 6(b). This is because the metal absorption is dominant for all these cases and this absorption increases when Re[ε] changes from -40 to -4.

(iv) For the dielectric mode, both the radiation loss and the metal absorption loss increase when $|\mathrm{Re}[\varepsilon]|$ decreases. As a result, the total Q factor degrades monotonically, as shown in Fig. 6(c).

Some typical noble metals fall within the simulated permittivity range. For example, at the wavelength of 680 nm, the permittivity of the most popular experimental coating metal silver is around $\varepsilon = -20.099 - 0.233i$, the permittivity of gold is around $\varepsilon = -14.16 - 1.069i$, and that of copper is about $\varepsilon = -14.10 - 1.65i$ [39]. From the results above, we can infer that for the exterior plasmonic mode at 680 nm, the maximum Q factor is around 1000 for the case of silver coating, while only about 200 for the case of gold coating when $R_1 = 10\ \mu$m, $R_2 = 1\ \mu$m, and $t = 100$ nm.

IV. Q FACTORS OF THE PLASMONIC MODES AT DIFFERENT WAVELENGTHS

From the results in Sec. III, we know that (i) the radiation losses of the modes depend dominantly on Re[ε] of the coating metal; (ii) the absorption losses rely on both the real and imaginary parts because the metal absorption ability is directly described by the latter, and the mode energy fraction in the coating-metal nanolayer is significantly related to the former. In this section, considering the coating metal of silver, we further study the Q factors of the fundamental exterior and interior plasmonic modes at different wavelengths. In this simulation, $R_1 = 10\ \mu$m, and the material dispersion of silver is also taken into account.

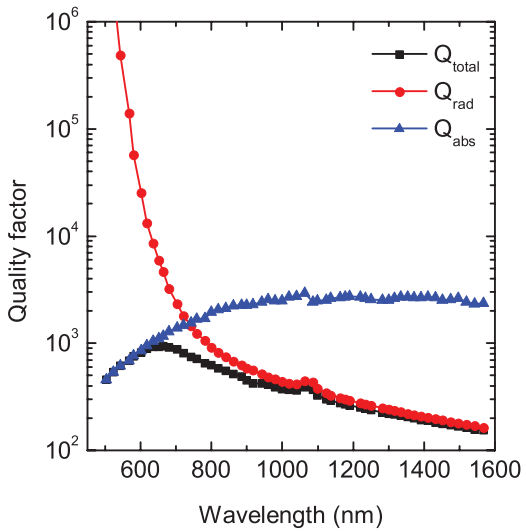

FIG. 7. (Color online) Numerically simulated radiation-related, absorption-related, and total Q factors Q_{rad}, Q_{abs}, and Q_{total} depending on the wavelength, for the fundamental exterior plasmonic mode. The major radius of the toroid is 10 μm.

A. Fundamental exterior plasmonic mode

We investigate the fundamental exterior plasmonic mode first with the radiation-related, absorption-related, and total Q factors shown in Fig. 7. It can be found that Q_{rad} degrades quickly from several millions to hundreds, while Q_{abs} increases monotonically from tens to hundreds, when the wavelength λ shifts from 500 to 1600 nm. As a result, Q_{total} is limited by the absorption loss at the short-wavelength band, while it depends mainly on the radiation loss at the longer wavelength.

First, the potential barrier at longer-wavelength band is much higher, as demonstrated in Fig. 8(a) where the potential barrier height at 1200 nm is more than four times higher than that at 600 nm. As the exterior plasmonic mode is distributed out of the cavity body, the mode photon is hard to tunnel into the metal nanolayer for a high potential barrier. This is demonstrated in Fig. 8(b) where the mode energy fraction in the metal nanolayer decreases rapidly from 25% to 2.5% when

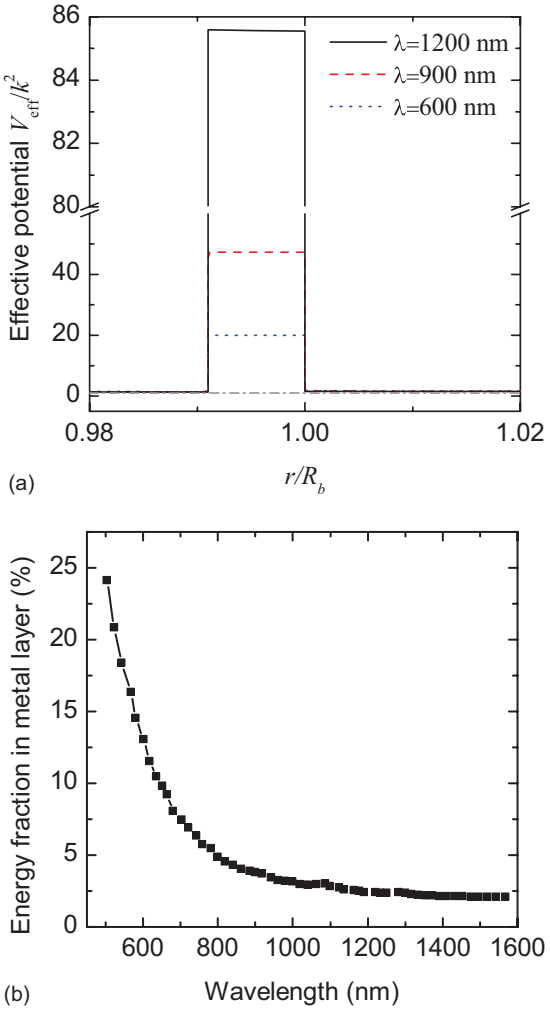

FIG. 8. (Color online) (a) Normalized effective potential V_{eff}/k^2 for the fundamental exterior plasmonic mode of a silver-coated microtoroid in water. The solid, dashed, and dotted lines are the effective potentials for $\lambda = 1200$, 900, and 600 nm. The dashed-dotted line shows the normalized photon energy k^2. (b) The mode energy percentage in the metal nanolayer for the exterior plasmonic mode.

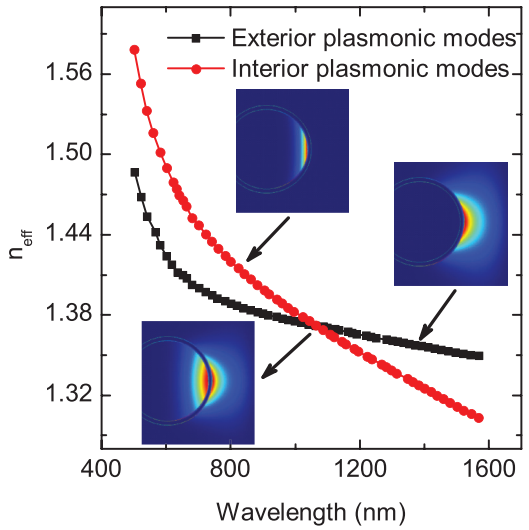

FIG. 9. (Color online) Effective mode indices for fundamental exterior and interior plasmonic modes in the silver-coated silica microtoroid. The three insets from top to bottom correspond to the mode profiles of the pure interior plasmonic mode, pure exterior plasmonic mode, and the asymmetric coupled mode. The mode indices meet each other at 1060 nm.

the wavelength moves from 500 to 1600 nm. The little energy tunneling into the metal nanolayer causes a small kinetic momentum of light, as shown in Fig. 9 where the effective mode index decreases rapidly at longer wavelength and approaches the refraction index of the surrounding medium. Therefore, photons tend to escape from the cavity due to the small momentum mismatching, and the Q_{rad} at short wavelength can be several-orders-of-magnitude higher than that at the long wavelength. This analysis is actually similar to that of Fig. 3 (red curve).

Second, as stated in the last paragraph, the mode energy fraction in the metal nanolayer decreases when the resonance moves to longer wavelength, resulting from the higher and higher potential barrier in this process. Thus, it is not surprising that we can expect a higher Q_{abs} at longer wavelength, by also noting the smaller imaginary part of the metal permittivity in this case.

Finally, due to the tradeoff between Q_{rad} and Q_{abs}, Q_{total} of the fundamental exterior plasmonic mode reaches its maximum at a certain wavelength. On the condition of $R_1 = 10\,\mu$m, the highest Q_{total} approaches 1000 at the optimal wavelength of ~680 nm. This optimal wavelength will blue-shift for a smaller-sized microcavity (by decreasing R_1).

In addition, we note that at the wavelength of 1060 nm in Fig. 7, both Q_{rad} and Q_{abs} have unusual change. This is because of the mode coupling between the fundamental exterior and interior plasmonic modes. The coupling produces two new eigenmodes: symmetric mode and asymmetric mode. For instance, the bottom inset in Fig. 9 shows the mode profile of the asymmetric mode due to the coupling. This kind of coupling occurs under the conditions of frequency resonance and phase matching. For the frequency resonance, it can be seen in Fig. 2 where the exterior and interior plasmonic modes have almost the same frequency around the mode number $m \sim 85$, i.e., $\lambda \sim 1060$ nm. For the phase-matching condition, Fig. 9 shows that the mode indices of the two kinds of modes vary with the wavelength. It can be found that the mode indices meet each other just at $\lambda \sim 1060$ nm.

B. Fundamental interior plasmonic mode

We now turn to study the fundamental interior plasmonic mode at different wavelengths. For this, Fig. 10(a) presents Q_{rad}, Q_{abs}, and Q_{total}. Different from the fundamental exterior plasmonic modes, Q_{total} of the interior mode depends mainly on the absorption originating from the coating metal, and the radiation loss plays a minor role except at 1060 nm where the mode coupling occurs. The high potential barrier resulting from the large negative real part of the metal permittivity prevents the photon from tunneling to the outside.

The Q_{rad} also exhibits a decrease and then an increase when the wavelength red-shifts. This can be explained similar to Fig. 3 (black curve). On one hand, a higher potential barrier at the longer wavelength leads to a reduced radiation loss. On the other hand, when the potential barrier is higher, the interior plasmonic mode is more difficult to tunnel into the metal nanolayer, as demonstrated in both Fig. 10(b) describing the energy fraction in metal and Fig. 9 studying the effective mode index. In this case, a small kinetic momentum of light boosts the radiation loss. Nevertheless, the Q_{rad} can reduce to several thousands in the 1060-nm band, which is also resulted

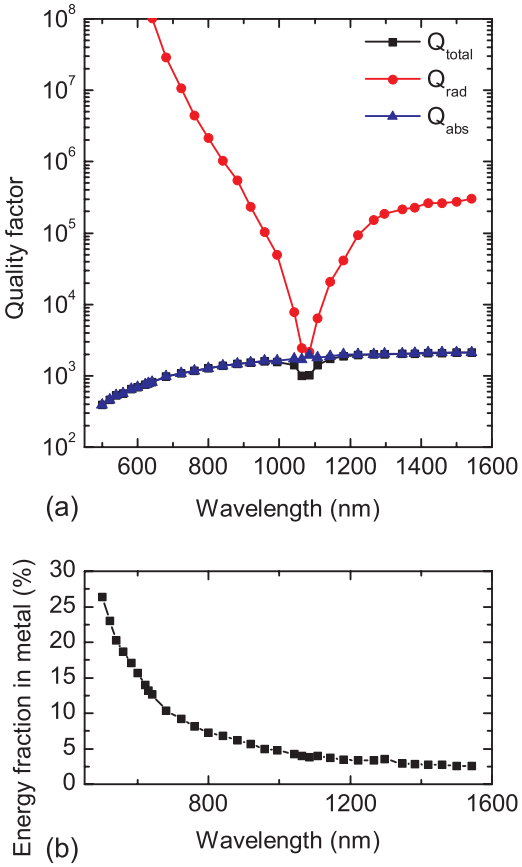

FIG. 10. (Color online) (a) Numerically simulated Q_{rad}, Q_{abs}, and Q_{total} depending on wavelength ranging from 500 to 1600 nm, for the fundamental interior plasmonic mode. The major radius of the toroid is 10 μm. (b) The energy fraction of the mode in the metal nanolayer.

from the mode coupling since the coupled exterior mode has a large radiation loss at this wavelength.

V. PLASMONIC MODES AND UNCOATED DIELECTRIC MODES AT DIFFERENT CAVITY SIZES

In this section, we probe into the effect of the cavity size on the mode Q factor since the effective potential depends partly on the cavity size. In Fig. 11, we plot Q_{total} of the exterior and interior plasmonic modes in the 680-nm band depending on R_1 of the cavity. It can be seen that both Q factors increase monotonically due to the reduced radiation loss when the microcavity expands. For instance, the Q factors of the exterior and interior modes are only 280 and 770 at $R_1 = 3\,\mu$m, while they improve to about 950 and 980 at $R_1 = 10\,\mu$m, respectively. Moreover, this increase saturates when the cavity is large enough because the Q factors are metal-absorption-limited in this case. In addition, when R_1 exceeds 12 μm, we find that Q_{total} of the exterior plasmonic mode is even slightly better than that of the interior mode. For example, Q_{total} reaches 1050 for the exterior mode, while it is about 1000 for the interior mode. This is attributed to the smaller metal absorption loss of the exterior mode.

One may argue that the Q factors of the plasmonic modes are much lower than that of a pure dielectric mode in the absence of the coating nanolayer. This is right when the cavity is large. However, when the cavity is small, desirable for compact photonic devices, both the interior and exterior plasmonic modes stand out their potential. To illustrate this, Fig. 11 also plots Q_{total} of the pure dielectric TE and TM polarized modes without metal coating in the same wavelength band. Remarkably, when the cavity is small enough, Q_{total} of the plasmonic modes exceed that of the pure dielectric mode. For instance, when $R_1 = 3\mu$m, Q_{total} reaches 280 for the exterior plasmonic mode and 780 for the interior plasmonic mode, while it is less than 80 for the pure dielectric mode without the metal-coating nanolayer. The potential reason for this phenomenon is that for a cavity with extremely small radius, Q of the cavity mode is mainly determined by the radiation loss, even for the interior or exterior plasmonic modes with large metal absorption. Meanwhile, metal also provides compact field confinement for these plasmonic modes, which can partly reduce the leakage of mode and is beneficial for stable circulation of light inside the mode volume.

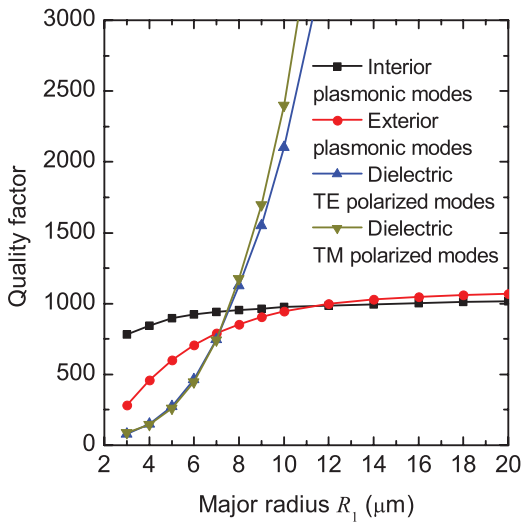

FIG. 11. (Color online) Total Q factors Q_{total} for the fundamental interior and exterior plasmonic modes of a silver-coated silica microtoroid depending on the major radius R_1, in the 680-nm band. For comparison, the total Q factors of the pure dielectric TE and TM polarized modes without the metal coating are also plotted in the same wavelength band.

VI. DISCUSSION AND CONCLUSION

We have investigated the confinement mechanisms and the resulting Q factors of the dielectric mode, exterior plasmonic mode, and interior plasmonic mode in a metal-coated silica microtoroid cavity. With the effective potential approach, we show that a larger negative value of real part of the coating-metal permittivity produces a higher potential barrier inside the resonator for all these modes, but results in different effects for them. For the exterior plasmonic mode, the lower effective potential barrier leads to better mode confinement. This is because in this case more mode energies can tunnel into the metal nanolayer. For the dielectric mode distributed in the silica core, however, a lower potential barrier causes a higher radiation loss of the mode and reduces the Q factor. For the interior plasmonic mode, on one hand, a lower potential barrier induces an increased radiation loss, similar to what occurred in the dielectric mode. On the other hand, the interior plasmonic mode turns to tunnel into the metal nanolayer when the potential barrier is low, which is helpful for suppressing the radiation, similar to the effect in exterior plasmonic mode.

The absorption loss is the other important decay pathway of the mode, which depends directly on the imaginary part of the metal permittivity and the energy fraction in the metal nanolayer. Importantly, this energy fraction relies on the mode confinement governed by the effective potential barrier of the metal nanolayer. As an example, we investigate the Q factors of the plasmonic modes at different wavelengths by considering the coating metal of silver. Moreover, we compare the plasmonic modes in the coated microcavity and the dielectric modes in the uncoated microcavity at different cavity sizes. An intriguing phenomenon is that the Q factors of the plasmonic modes exceed significantly that of the uncoated dielectric modes, when the cavity is small enough which is highly desirable for compact photonic devices.

ACKNOWLEDGMENTS

This work was supported by the National Key Basic Research Program of China (Grant No. 2013CB328704), the National Natural Science Foundation of China (Grants No. 61077027, No. 11134001, No. 11121091, and No. 90921008). The authors acknowledge Professor Y.-F. Xiao for very useful discussions.

APPENDIX

As the microtoroid structure we studied is axisymmetric, we can study the optical properties of such a cavity structure in cylindrical coordinates $\{r,\phi,z\}$. Generally, the electromagnetic

field can be expressed by

$$\Psi(r,\phi,z) = \sum_{m=-\infty}^{+\infty} C_m \Phi_m(r,z) e^{im\phi - i\omega t},$$

where m is the angular momentum (azimuthal mode number), ω is the frequency, $\Phi_m(r,z)$ denotes the field profile at the cross section and C_m is the coefficient. For a given m, the corresponding eigenmodes should satisfy the character equation

$$\nabla^2_{r,z}\Phi_m(r,z) - m^2\Phi_m(r,z) + \varepsilon\left(\frac{\omega}{c}\right)^2 \Phi_m(r,z) = 0,$$

with ε the relative permittivity. The eigenfrequency and mode profile can be solved by applying the boundary conditions to this equation.

Since there is no analytical solution to the toroid-shaped boundary, we solve the partial differential equation (PDE) numerically by finite-element method (FEM) with a commercial available software ("weak form, boundary" module in COMSOL MULTIPHYSICS 3.5A). More details of the "weak form" of axisymmetric Maxwell equations can be found in [38]. Usually, the imperfect boundary conditions of a finite domain will introduce errors to the simulations. For example, outgoing light waves may be reflected at the domain boundary. Thus, we introduce the perfect matched layers (PML) outside the calculation regions to improve the simulation accuracy.

By solving the eigenmodes for a given m, we can get the eigenfrequency ω_m and the corresponding electric and magnetic field patterns $[\Phi_m(r,z)]$ of the whispering-gallery modes at the cross section of this metal-coated microtoroid.

The Q factor of whispering-gallery modes can be computed through $Q = |\mathrm{Re}(\omega_m)/2\,\mathrm{Im}(\omega_m)|$. The energy fraction in metal is defined as $\eta = W_{\mathrm{metal}}/W_{\mathrm{total}}$, where

$$W_{\mathrm{metal/total}} = \iint_{\mathrm{metal/total}} 2\pi r \times \mathrm{Re}\left\{\frac{d[\epsilon(r)\omega]}{d\omega}|E(r)|^2 + \mu_0|H(r)|^2\right\} dr\,dz$$

denotes the electromagnetic energy in metal and the whole area, with the electric and magnetic fields $E(r)$ and $H(r)$, and the permeability of vacuum μ_0. All these quantities can be obtained through the postprocessing procedure.

[1] W. L. Barnes, A. Dereux, and T. W. Ebbesen, Nature (London) **424**, 824 (2003).
[2] H. Raether, *Surface Plasmons on Smooth and Rough Surfaces and on Gratings* (Springer, Berlin, 1988).
[3] E. Ozbay, Science **311**, 189 (2006).
[4] M. L. Brongersma and P. G. Kik, *Surface Plasmon Nanophotonics* (Springer, Dordrecht, 2007).
[5] S. Nie and S. R. Emery, Science **275**, 1102 (2007).
[6] K. Kneipp, Y. Wang, H. Kneipp, L. T. Perelman, I. Itzkan, R. R. Dasari, and M. S. Feld, Phys. Rev. Lett. **78**, 1667 (1997).
[7] D. Wang, W. Zhu, Y. Chu, and K. B. Crozier, Adv. Mater. **24**, 4376 (2012).
[8] E. Fort and S. Grésillon, J. Phys. D: Appl. Phys. **41**, 013001 (2008).
[9] F. Tam, G. P. Goodrich, B. R. Johnson, and N. J. Halas, Nano Lett. **7**, 496 (2007).
[10] T. Liebermann and W. Knoll, Colloids Surf. A **171**, 115 (2000).
[11] B. Liedberg, C. Nylander, and I. Lunström, Sens. Actuators **4**, 299 (1983).
[12] J. Homola, Chem. Rev. **108**, 462 (2008).
[13] M. Piliarik, P. Kvasnička, N. Galler, J. R. Krenn, and J. Homola, Opt. Express **19**, 9213 (2011).
[14] N. Verellen, P. V. Dorpe, C. Huang, K. Lodewijks, G. A. E. Vandenbosch, L. Lagae, and V. V. Moshchalkov, Nano Lett. **11**, 391 (2011).
[15] J. N. Anker, W. P. Hall, O. Lyandres, N. C. Shah, J. Zhao, and R. P. Van Duyne, Nat. Mater. **7**, 442 (2008).
[16] H. Ditlbacher, A. Hohenau, D. Wagner, U. Kreibig, M. Rogers, F. Hofer, F. R. Aussenegg, and J. R. Krenn, Phys. Rev. Lett. **95**, 257403 (2005).
[17] H. T. Miyazaki and Y. Kurokawa, Phys. Rev. Lett. **96**, 097401 (2006).
[18] J.-C. Weeber, A. Bouhelier, G. C. des Francs, L. Markey, and A. Dereux, Nano Lett. **7**, 1352 (2007).
[19] E. J. R. Vesseur, R. de Waele, H. J. Lezec, H. A. Atwater, F. J. García de Abajo, and A. Polman, Appl. Phys. Lett. **92**, 083110 (2008).
[20] J.-C. Weeber, Y. Lacroute, A. Dereux, E. Devaux, T. Ebbesen, C. Girard, M. U. González, and A.-L. Baudrion, Phys. Rev. B **70**, 235406 (2004).
[21] Z. W. Liu, Q. H. Wei, and X. Zhang, Nano Lett. **5**, 957 (2005).
[22] B. Wang and G. P. Wang, Appl. Phys. Lett. **87**, 013107 (2005).
[23] Y. Gong and J. Vučković, Appl. Phys. Lett. **90**, 033113 (2007).
[24] A. Kocabas, S. Seckin Senlik, and A. Aydinli, Phys. Rev. B **77**, 195130 (2008).
[25] C. E. Hofmann, E. J. R. Vesseur, L. A. Sweatlock, H. J. Lezec, F. J. García de Abajo, A. Polman, and H. A. Atwater, Nano Lett. **7**, 3612 (2007).
[26] V. J. Sorger, R. F. Oulton, J. Yao, G. Bartal, and X. Zhang, Nano Lett. **9**, 3489 (2007).
[27] A. Vardanyan, H. Haroyan, A. Babajanyan, K. Nerkararyan, and B. Friedman, Plasmonics **7**, 1 (2012).
[28] S.-H. Kwon, Opt. Express **20**, 24918 (2012).
[29] A. Vardanyan, H. Haroyan, A. Babajanyan, K. Nerkararyan, K. Lee, and B. Friedman, J. Appl. Phys. **111**, 053112 (2012).
[30] S. I. Bozhevolnyi, V. S. Volkov, E. Devaux, J.-Y. Laluet, and T. W. Ebbesen, Nature (London) **440**, 04594 (2006).
[31] T. J. Kippenberg, J. Kalkman, A. Polman, and K. J. Vahala, Phys. Rev. A **74**, 051802(R) (2006).
[32] M. Borselli, T. J. Johnson, and O. Painter, Opt. Express **13**, 1515 (2005).
[33] B. Min, E. Ostby, V. Sorger, E. Ulin-Avila, L. Yang, X. Zhang, and K. Vahala, Nature (London) **457**, 455 (2009).
[34] Y.-F. Xiao, C.-L. Zou, B.-B. Li, Y. Li, C.-H. Dong, Z.-F. Han, and Q. Gong, Phys. Rev. Lett. **105**, 153902 (2010).
[35] D. K. Armani, T. J. Kippenberg, S. M. Spillane, and K. J. Vahala, Nature (London) **421**, 925 (2003).

[36] K. J. Vahala, Nature (London) **424**, 839 (2003).
[37] S. M. Spillane, T. J. Kippenberg, K. J. Vahala, K. W. Goh, E. Wilcut, and H. J. Kimble, Phys. Rev. A **71**, 013817 (2005).
[38] M. Oxborrow, IEEE Trans. Microwave Theory Tech. **55**, 1209 (2007).
[39] P. B. Johnson and R. W. Christy, Phys. Rev. B **6**, 4370 (1972).
[40] E. D. Palik, *Handbook of Optical Constants of Solids* (Academic, New York, 1985).
[41] G. M. Hale and M. R. Querry, Appl. Opt. **12**, 555 (1973).
[42] M. Daimon and A. Masumura, Appl. Opt. **46**, 3811 (2007).
[43] N. Engheta and R. W. Ziolkowski, *Metamaterials: Physics and Engineering Explorations* (Wiley, New York, 2006).
[44] B. R. Johnson, J. Opt. Soc. Am. A **10**, 343 (1993).